

Multiscale characterization of damage tolerance in barium titanate thin films


Cite as: J. Appl. Phys. **132**, 045302 (2022); <https://doi.org/10.1063/5.0095139>

Submitted: 08 April 2022 • Accepted: 01 July 2022 • Published Online: 26 July 2022

 N. G. Mathews,  A. K. Saxena, N. Venkataramani, et al.

COLLECTIONS

Paper published as part of the special topic on [Advances in Multi-Scale Mechanical Characterization](#)

 This paper was selected as Featured



View Online



Export Citation



CrossMark

ARTICLES YOU MAY BE INTERESTED IN

[Phase transition by nanoindentation in a relaxor ferroelectric single crystal PMN-0.3PT: A phase-field investigation](#)

Journal of Applied Physics **131**, 244101 (2022); <https://doi.org/10.1063/5.0090419>

[Volumetric tri-modal imaging with combined photoacoustic, ultrasound, and shear wave elastography](#)

Journal of Applied Physics **132**, 034902 (2022); <https://doi.org/10.1063/5.0093619>

[Dynamic adhesion of 2D materials to mixed-phase BiFeO₃ structural phase transitions](#)

Journal of Applied Physics **132**, 045301 (2022); <https://doi.org/10.1063/5.0096686>

Journal of Applied Physics **Special Topics** Open for Submissions [Learn More](#)

Multiscale characterization of damage tolerance in barium titanate thin films

Cite as: J. Appl. Phys. **132**, 045302 (2022); doi: [10.1063/5.0095139](https://doi.org/10.1063/5.0095139)

Submitted: 8 April 2022 · Accepted: 1 July 2022 ·

Published Online: 26 July 2022



View Online



Export Citation



CrossMark

N. C. Mathews,¹  A. K. Saxena,^{2,a)}  N. Venkataramani,¹ G. Dehm,²  and B. N. Jaya^{1,b)} 

AFFILIATIONS

¹Department of Metallurgical Engineering and Materials Science, Indian Institute of Technology Bombay, Mumbai 400076, India

²Department of Structure and Nano-/Micromechanics of Materials, Max-Planck-Institut für Eisenforschung GmbH, Max-Planck-Strasse 1, Düsseldorf 40237, Germany

Note: This paper is part of the Special Topic on Advances in Multi-Scale Mechanical Characterization.

a) Present address: Centre for Innovative Manufacturing Research, Vellore Institute of Technology, Vellore 632014, India

b) Author to whom correspondence should be addressed: jayabalila@iitb.ac.in

ABSTRACT

Barium titanate is a brittle, lead free ferroelectric and piezoelectric ceramic used in patterned and thin film forms in micro- and nano-scale electronic devices. Both during deposition and eventually during service, this material system develops stresses due to different loads acting on the system, which can lead to its failure due to cracking in the films and/or interface delamination. *In situ* microcantilever bending based fracture experiments and tensile tests based on shear lag tests in combination with digital image correlation were used to understand the cracking behavior of barium titanate films when deposited on flexible substrates. For the first time, the fracture behavior of these nanocrystalline barium titanate films has been quantified in terms of fracture toughness, fracture strength, and interface shear stresses for different film thicknesses. Critical defect size is estimated using the above information as a function of film thickness. It is found that damage tolerance in terms of fracture strength depends on film thickness. Furthermore, compared to a bulk single crystal, barium titanate fracture resistance of the nanocrystalline thin films is reduced. Both effects need to be considered in engineering design of reliable devices employing micro- and nano-scale barium titanate thin film structures.

Published under an exclusive license by AIP Publishing. <https://doi.org/10.1063/5.0095139>

I. INTRODUCTION

The drive towards miniaturization of devices for more robust and reliable applications mandates the estimation of deformation and fracture behavior in the relevant length scales of application. Most functional micro-electronic mechanical systems (MEMS) use ferroelectric/piezoelectric ceramics like barium titanate (BaTiO_3) as sensors and actuators in their bulk and nanostructured thin film forms.¹ BaTiO_3 is intrinsically brittle in its bulk form; therefore, damage tolerance is critical to their deployment in service and life extension. Micropillar compression experiments on single crystal BaTiO_3 revealed a size effect in yield strength with pillars less than $1\ \mu\text{m}$ diameter reaching near theoretical strengths.² As a consequence, the elastic strain limit was also pushed to significantly higher values with decrease in size, followed by accommodation of strain through dislocation mediated plasticity.² While this is true for single crystals, there are very few reports of the mechanical

behavior of nanocrystalline thin films of BaTiO_3 grown through different physical, chemical, and electrochemical methods. Various deposition techniques such as sputtering, pulsed laser deposition (PLD), chemical vapor deposition (CVD), solgel process, and hydrothermal process have been reported in the literature.³ PLD allows the growth of oxide thin films over higher oxygen partial pressures, which decrease the oxygen vacancy concentration in the film.^{4,5} BaTiO_3 has been deposited on a variety of substrates including SrTiO_3 , Ni, and Si, using $\text{Ba}_x\text{Sr}_{1-x}\text{TiO}_3$, LaNiO_3 , and SrRuO_3 buffer layers to achieve epitaxy, while thicker films up to $1\ \mu\text{m}$ thickness have also been successfully grown recently by PLD.⁶⁻⁸ There have been efforts in the recent past to utilize the piezoelectric property of BaTiO_3 thin films in the development of flexible electronic systems.^{9,10} Failure in BaTiO_3 thin films happens especially due to tension developing during bending, which ruptures the films in a brittle manner. Therefore, the tendency for cracking of these thin films on different flexible substrates were studied using

shear lag tension, as this technique allows for quantitative measurements without the need for making free-standing specimens.^{11–13}

The fracture behavior in brittle thin films is quantified in terms of fracture strain, fracture strength, fracture energy, or fracture toughness. Different micromechanical experiments have been performed to understand the fracture behavior in different classes of thin film materials.¹⁴ *In situ* tensile test on the film/substrate system based on the shear lag model is one such approach to measure fracture stress of thin films and also their adhesion energies and interface shear strengths.^{11,15,16} These *in situ* tensile tests are also a reliable screening technique to compare the fracture toughness in brittle and hard coatings using the fracture strain criteria.^{17–19} For ceramic (film)/metal (substrate) system, the plastic deformation in the metal substrate (as a result of application of strain) is accommodated by the elastic deformation of the ceramic film until the film cracks. The strain at which the film cracks is used to determine its fracture strength (σ_f). The following two conditions are assumed during the calculation of fracture strength—(i) film behaves in an elastic manner until fracture and (ii) film ruptures before the decohesion failure of the interface. On the other hand, single edged notched microcantilever is a widely used reliable geometry for fracture toughness (K_{IC}) measurements of free-standing thin films and multilayers.^{20–23} It was shown in our previous study that microcantilever beam with a length (L) to width (W) ratio larger than 4 ensures dominant mode I loading and measurement of K_{IC} .²⁴ The critical load at which the cantilever fractures is used to estimate the fracture toughness in systems that display linear elastic behavior until fracture. However, the sample preparation is time and energy intensive, usually requiring a focused ion beam (FIB) to make the cantilever free-standing.

In this study, the fracture behavior of BaTiO₃ thin films is studied in their stress-free free-standing form as well as residually stressed form when they are attached to a flexible metallic substrate. The former is achieved through microcantilever fracture tests and the latter through shear lag tests. The stress-free form is deposited on Pt–Si substrates since thicker films could be grown on them without microcracks, while the residually stressed forms were deposited on Ni substrates to enable shear lag tests. The damage tolerance is quantified in BaTiO₃ films on Ni substrates using the crack density–strain curve to determine the onset of cracking. Fracture stress and interface stress of the BaTiO₃/Ni (ceramic/metal) system for different film thickness are estimated from *in situ* tensile tests utilizing the strain at the onset of cracking and the mean crack spacing. In addition, the regions of localized strain accumulation in BaTiO₃ films on Ni substrates during the tests are measured by full field digital image correlation (DIC) to determine the cracking location and propensity.

II. EXPERIMENTAL METHODOLOGY

A. Deposition and microstructural characterization of BaTiO₃ thin films

BaTiO₃ target for PLD technique was made in the form of a pellet by conventional solid state reaction process using BaCO₃ and TiO₂ powders. BaCO₃ and TiO₂ powders (procured from Sigma Aldrich) were initially heated to 200 °C to remove the moisture. These were then mixed in the required stoichiometric molar ratio

(BaCO₃:TiO₂ = 1:1) and ground well using a mortar and a pestle. Furthermore, ball milling was performed for 12 h. The mixed powder was then calcined at 1100 °C for 4 h to facilitate the formation of BaTiO₃. The calcined powder was analyzed by x-ray diffraction (XRD) to confirm the formation of single phase tetragonal BaTiO₃. This calcined powder was again ground further and a few drops of poly vinyl acetate were added as a binder. The mixture was then pressed in a hydraulic press at a pressure of 200 MPa to obtain the green pellet. Final sintering of the pellets was carried out at 1400 °C for 4 h in a high temperature muffle furnace to yield 96% of the theoretical density. Phase purity of both BaTiO₃ powders and the sintered pellet was confirmed by x-ray diffraction (XRD) measurements using CuK α ($\lambda = 0.154$ nm) radiation; all indexed peaks corresponded to single phase BaTiO₃. Lattice parameters and tetragonality (c/a ratio) calculated from measured XRD peak positions of powdered and sintered BaTiO₃ are close to the theoretical values ($c = 0.403$ nm, $a = 0.399$ nm and $c/a = 1.01$). Density of the sintered BaTiO₃ pellet was measured by Archimedes principle using a water bath arrangement as per the ASTM C20-00 standard.²⁵ The as-received Ni substrates of 300 μ m thickness were polished using different grades of SiC polishing paper (up to 2000 grit size). Final polishing was performed with diamond paste (grit size of 0.5 μ m). The surface roughness of Ni substrates was measured to be within 20 nm. These polished samples were ultrasonically cleaned in ethanol and isopropyl alcohol before deposition. BaTiO₃ thin films were grown on Ni and Pt–Si substrates by the PLD technique using a KrF excimer laser (Lambda Physik) of 248 nm wavelength. Similar deposition conditions were used to grow films on both the Ni and Pt–Si substrates. A directional plasma plume, which provides the material flux, was generated by focusing the laser onto the surface of the target. A laser fluence of 2.5 J/cm² with a laser pulse repetition rate of 3 Hz was used for depositions. Film thickness was controlled by varying the number of laser pulses. The substrates were mounted on a rotating holder at a distance 4.5 cm away from the target, normal to the plume direction. During deposition, substrate temperature was maintained at 700 °C, and after deposition, different cooling steps of 1 °C/min up to 650 °C and 3 °C/min up to 300 °C were followed, which reduced the formation of cracks in the film. Oxygen at partial pressure of 100 mTorr was supplied inside the chamber during deposition, which aids to obtain the required stoichiometry of the BaTiO₃ film. Films of thicknesses (h) 300, 600, and 900 nm were deposited on Ni substrates which are pre-machined to the shape of a tensile specimen. The grip section of the specimen was masked using pieces of silicon wafers to create a shear lag specimen.

After deposition, phase purity of the thin films was inspected by grazing incidence (GI) XRD at an incidence angle of 0.5° using CuK α radiation, and the peaks corresponding to tetragonal BaTiO₃ were indexed confirming the polycrystalline nature of all the films deposited. These XRD peak positions of thin films in comparison with stress-free powder samples were used for a first approximation to estimate residual stresses (σ_r) in the films as given in Eq. (1). E and ν represent the elastic modulus and Poisson's ratio, respectively. The lattice strain measurements were carried out from the corresponding d -spacings (represented as d_o for stress-free powder and d_f for the thin films) of the powder and thin films. The tetragonality of these thin films was also confirmed from Raman

spectroscopy measurements,

$$\sigma_r = -\left(\frac{d_f - d_o}{d_o}\right)\left(\frac{E}{1-\nu}\right)_f. \quad (1)$$

Elastic modulus of the film (E_f) was measured using nanoindentation (Bruker TI Premier) on films of $\sim 1\text{--}1.5\ \mu\text{m}$ thickness deposited on Ni and Pt-Si substrates using a diamond Berkovich tip of 100 nm radius, through the standard Oliver-Pharr method.²⁶ The indentations were done at a fixed load of 5 mN, reaching a maximum depth of ~ 200 nm, within 10% of the film thickness. The average surface roughness of BaTiO₃ films deposited on both Pt-Si and Ni was less than 20 nm. Since the indentation depth exceeded the surface roughness of the films by ten times, the measurements were assumed to be not influenced by the same.

B. Microcantilever bending based fracture test of free-standing film

Microcantilevers were fabricated from BaTiO₃ thin film samples of $\sim 1.5\ \mu\text{m}$ thickness deposited on Pt-Si substrate. The substrates were ultrasonically cleaned in ethanol before deposition. Free-standing single edge notched microcantilevers were milled from the nanocrystalline thin film samples using FIB (Zeiss Auriga® Compact). The milling parameters are described elsewhere and hence not repeated here.²⁴ The microcantilevers were of thickness (h) $\sim 1.5\ \mu\text{m}$, width (B) $\sim 1.5\ \mu\text{m}$, and beam aspect ratio (L/h) ~ 5 , with notches of notch depth ratio (a/h) of approximately 0.4 introduced at $x/h \approx 1$ from the fixed end of the cantilever [see Fig. 1(a) for definition of L , h , a , and x]. The Ga ion implantation near the notch tip was minimized by selecting the lowest possible current of 10 pA during notching. The geometrical conditions were selected to ensure dominant mode I loading at the crack tip.²⁴ Microcantilever fracture experiments were performed *in situ* inside a scanning electron microscope (SEM) (Zeiss Gemini 500) using an indenter (ASMEC—UNAT II) equipped with diamond wedge tip $10\ \mu\text{m}$ width by loading close to the free end of the cantilever in displacement control mode with a displacement rate of 5 nm/s. Fracture toughness (K_{IC}) of the material was calculated from the maximum load (P_{crit}) at fracture [Fig. 1(b)] and is quantified using Eqs. (2) and (3),²⁴

$$K_{IC} = \frac{P_{crit} L}{Bh^{1.5}} f\left(\frac{a}{h}\right), \quad (2)$$

$$f\left(\frac{a}{h}\right) = -3.15 + 72.85\left(\frac{a}{h}\right) - 188.51\left(\frac{a}{h}\right)^2 + 202.61\left(\frac{a}{h}\right)^3. \quad (3)$$

C. Shear lag test of the film-substrate system

To estimate the strain to cracking (ϵ_f) and fracture strength (σ_f) of BaTiO₃ thin films deposited on Ni substrates, tensile tests based on the shear lag model were used. The film is deposited only on the gauge section while the grip is only of the nickel (Ni) substrate, so that the load transfer occurs through the interface. *In situ* tests were performed on the BaTiO₃-Ni film-substrate system in the form of tensile shaped specimen geometry [Fig. 1(c)], using the

microtensile testing device (Gatan Ltd.) inside a scanning electron microscope (SEM) (Zeiss Auriga® Compact). Samples were mounted in between the grips of the tensile module equipped with a 5 kN load cell, and pulled at a displacement rate of 0.1 mm/min. Tensile test was interrupted in between at every 0.01 mm displacement of the cross-head [Fig. 1(d)], and the corresponding SEM images were captured at a fixed magnification, until the failure of the Ni substrate. Three samples of each film thickness were considered for the *in situ* tests. Cracks perpendicular to the loading direction were observed in films during straining of the sample, and the strain at which the first crack was observed is noted as ϵ_f for the onset of cracking. Crack densities were measured from the captured SEM images using the line intercept method. Multiple lines of known length were drawn on the SEM images and the numbers of crack intercepts were counted; crack density was calculated as the number of intercepts divided by the total length of the line. Actual strains experienced by the film were measured using the digital image correlation (DIC) technique (VIC 2D software) using the captured SEM images. The microstructure morphology of the film surface acted as markers for the DIC analysis to calculate strains. DIC measures the actual strain in the film avoiding the machine compliance issues in the measurement of strain from the cross-head displacement. Fracture strength was estimated from Eq. (4) assuming that the film is elastic until fracture,

$$\sigma_f = E_f \epsilon_f. \quad (4)$$

The interface shear strength of the metal ceramic interface was estimated by the periodic cracking technique developed by Agrawal and Raj.¹³ After the onset of fracture, the in-plane stresses in the film are transferred to the interface as shear stresses near the free edge of the crack. The cracking density reaches a plateau upon further straining, and the maximum interface shear traction (τ_{ISS}) was determined by measuring the average crack spacing (λ_{avg}) at crack saturation strain using Eq. (5),²⁷⁻²⁹

$$\tau_{ISS} = \frac{3}{4}\pi \frac{h}{\lambda_{avg}} \sigma_f. \quad (5)$$

III. RESULTS AND DISCUSSION

A. Microstructure characterization of as-deposited films

XRD characterization of all the films showed their polycrystalline nature without any preferred orientation. Figure 2(a) shows the representative XRD profile for the BaTiO₃ films on the Pt-Si and Ni substrates. The XRD pattern revealed the polycrystalline nature of the films deposited on both substrates and the absence of texture with intensity profiles being similar. The FWHM was used to determine the grain size, which confirms their nano crystallinity and indicates a grain size of less than 60 nm. The peak broadening due to the nanocrystalline nature of the films camouflages the peak splitting that is seen for a tetragonal phase. The full width at half maximum of (110) and (111) peaks was used to estimate the grain size of the films using the Scherrer formula.³⁰ This was found to be nearly constant for all film thicknesses deposited on Ni, in the

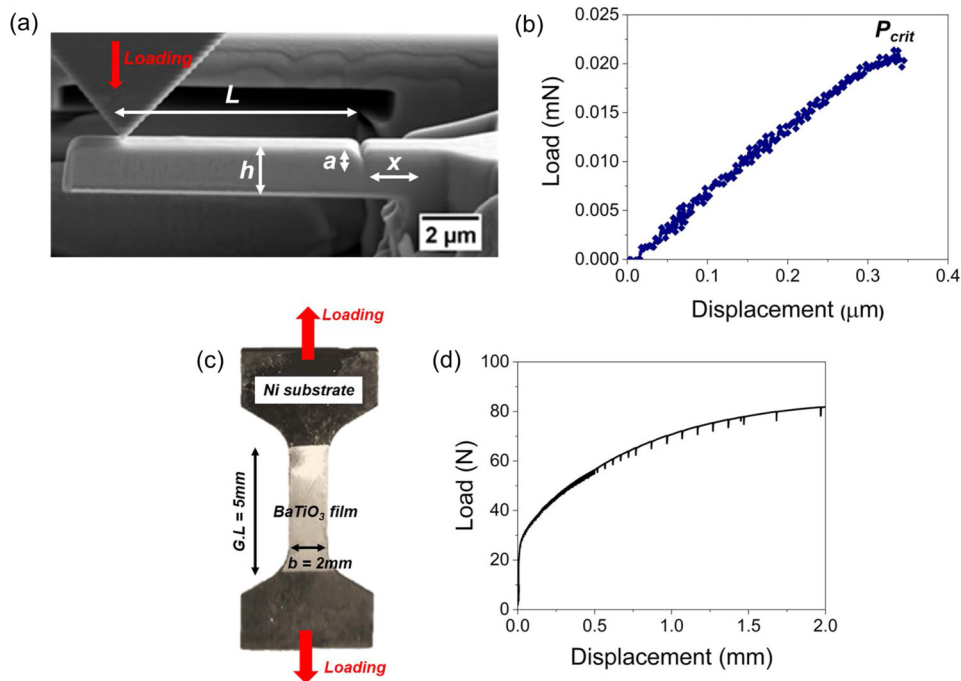


FIG. 1. (a) Single edge notched microcantilever geometry milled from polycrystalline BaTiO_3 thin film on the Pt-Si substrate, and (b) representative load-displacement curve during the microcantilever bend test. (c) Geometry and dimensions of the BaTiO_3 -Ni film-substrate sample used for shear lag tests, and (d) representative load-displacement curve during the *in situ* tensile tests.

range of $\sim 57 \pm 8$ nm. Few peaks of the substrates (Ni, Si, and Pt) were also observed in the profile, which overlap with the peaks of BaTiO_3 . Therefore, the non-overlapping (110) peak of BaTiO_3 was compared in the powder and thin film samples to estimate the residual strains present in the films. Figure 2(b) shows the comparison of peak positions of the (110) or (101) planes with respect to the powder. No peak shift was observed among the thin films of different thicknesses indicating similar strains in all the films. In comparison to the stress-free powder sample, all of the peaks showed a left-shift in 2θ , indicating a compressive in-plane residual stress Eq. (1). The $d\text{-sin}^2\psi$ technique was used to estimate a compressive residual stress of -550 MPa independent of the film thickness. Similar magnitudes have been reported for other thin films deposited by PVD routes in the literature.^{12,17}

The elastic modulus values averaged over ten indents result in an $E_f = 112 \pm 6$ GPa (standard error) for films deposited on Ni and $E_f = 107 \pm 2$ GPa for films on Pt-Si which are not very different from each other. This, along with the overlap of the XRD peaks, indicates that the deposited films are microstructurally similar. The elastic modulus for thin films (~ 112 GPa) were found to be significantly lower than the bulk (100) single crystal value (~ 150 GPa) and found to be closer to sintered polycrystalline BaTiO_3 (~ 110 GPa).³¹ The difference in elastic modulus between the single crystal and thin films could be due to the growth defects present in the film as well as the elastic anisotropy in the material, which are discussed later. The fact that the modulus of bulk polycrystalline BaTiO_3 is comparable to that of the thin film suggests that there is no substrate effect playing a role.

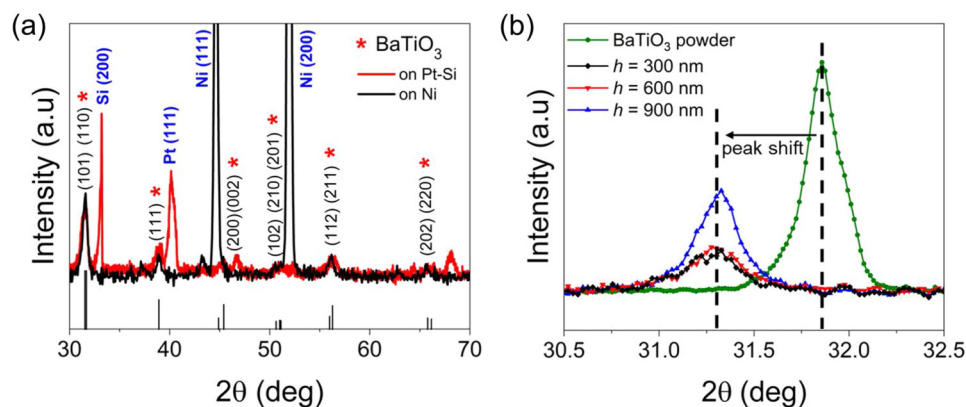


FIG. 2. (a) GI-XRD profile of BaTiO_3 thin films on Pt-Si and Ni substrates showing their polycrystalline nature and the absence of preferred orientation. (b) XRD peak corresponding to BaTiO_3 (110) plane of the powder sample compared to all three thin film samples of different thicknesses to determine the peak shift and residual stress.

B. Determination of fracture toughness of free-standing film

Fracture toughness values of thin film samples were determined from notched microcantilever bending based fracture experiments using Eqs. (2) and (3). Critical loads for fracture of at least five microcantilevers were measured from their corresponding load–displacement curves [Fig. 1(b)]. In order to have plane strain conditions in the sample, the minimum sample width B should be $\geq \sim 350$ nm according to Eq. (6). In our case, the sample width is ~ 1.5 μm , which is much beyond the minimum value. Therefore, plane strain conditions are satisfied in the fracture experiments,

$$B = 2.5 \left(\frac{K_{IC}}{\sigma_{ys}} \right)^2. \quad (6)$$

Post-fracture images were analyzed to identify the nature of fracture and also to measure the exact notch depth to calculate the fracture toughness (Fig. 3). It was evident from the linear elastic behavior of the load displacement curve until fracture and from the cleavage fracture features along the weak intercolumnar boundaries that the BaTiO₃ films fracture in a brittle manner. There was no crack kinking or deflection observed during fracture. The average K_{IC} of polycrystalline thin film BaTiO₃ was measured to be 0.4 ± 0.03 MPa $\sqrt{\text{m}}$. This is approximately 67% less in comparison to bulk single crystals of BaTiO₃,³² which is attributed to the columnar nature of the nanocrystalline thin films and the presence of defects and microcracks during the deposition process in the film. The K_{IC} measured here is a stress-free, truly microstructure dependent value, since the cantilever is free from the substrate and, therefore, free from residual stresses. All the thin films shown in this study are nanocrystalline without any texture. In case of single crystals, Brinckmann *et al.* reported that elastic anisotropy has less than 5% influence on the stress intensity factor for materials with a moduli ratio significantly less than 3.³³ In copper, the modulus ratio between E_{100} and E_{011} lies in the range 2–3, and hence the anisotropy may have significant influence on the fracture toughness.³⁴ In the tetragonal single crystal BaTiO₃ (100), the ratio of

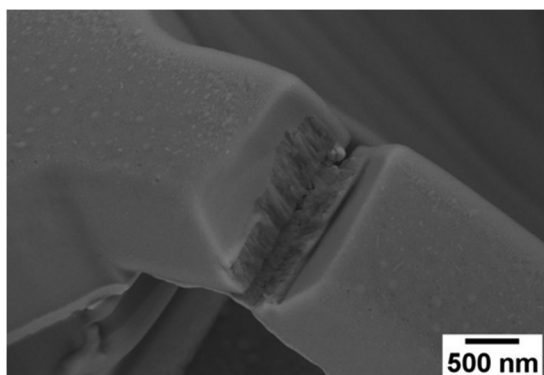


FIG. 3. Post-fracture image of the BaTiO₃ thin film microcantilever showing the brittle failure.

E_{100}/E_{011} is 1.29 and E_{100}/E_{001} is 1.06, which is well below 3. Hence, for BaTiO₃, crystal anisotropy is not expected to have a significant influence on the fracture toughness of single crystals, nor a cause for the difference in fracture toughness between the thin films and the single crystal. Porosities are known to deteriorate the fracture properties of polycrystalline ceramics, as also reported by Gong *et al.*³⁵ Hence, we believe that the difference in fracture toughness is essentially due to microstructural growth defects and pores in the thin films that are absent in the single crystal.

The residual stress and fracture toughness of the thin film was used to determine the critical film thickness h_{cr} for spontaneous delamination according to Eq. (7).³⁶ h_{cr} was found to be 1.1 μm . All the films deposited were lower than this and, therefore, had good adherence with the substrate for shear lag tests,

$$h_{cr} = \frac{2 K_{IC}^2}{\sigma_r^2}. \quad (7)$$

C. Fracture strength and critical strain for film cracking using shear lag tests

Analysis of strain maps obtained from DIC measurements revealed the regions of localized strain accumulation during the test. Cracks initiated from these regions of maximum strain accumulation. Figures 4(a) and 4(b) show the strain maps plotted just before and at the critical fracture strain values for the 300 and 900 nm thick films, respectively. The applied strain was reported as the area average value of strains from all positions inside the selected region. Initiation of cracks occurred from regions where the localized strains were 35%–55% greater than the average strains for 300 and 600 nm films, whereas the ratio was only 12% higher for 900 nm films. However, for the 900 nm films, these points of strain localization did not coincide with cracking and instead were initiated from pre-existing defects, which were not in the field of view. The critical strain at fracture determined from shear lag experiments revealed that the thicker film ($h = 900$ nm) has low damage tolerance compared to thinner films ($h = 300$ and 600 nm). More widely separated cracks were formed in the 900 nm films [Figs. 5(a) and 5(b)], which also showed a decreased crack density during straining. The minimum and maximum crack spacings were found to be within a factor of 2, and hence the shear lag assumption was found to be valid.¹⁶ The interface shear stress calculated from Eq. (5) showed that thinner films have higher interfacial shear strength compared to the 900 nm film. With increase in strain values beyond the saturation strains, secondary cracks were generated, which connected the existing primary cracks. This led to buckling and interface delamination [Figs. 5(a) and 5(b)] of the films in all cases.

Figure 6(a) shows the plot of crack density vs strain for different film thicknesses at different intervals of strain, while Fig. 6(b) shows the distribution of crack spacing measured at saturation strains. The crack spacing distribution was found to be narrower for the 900 nm films, indicating the predominant role of defects in them. Since pre-existing defect sites acted as crack initiators, there were not many new cracks nucleated with strain and the distribution saturated very quickly. The crack opening instead was larger

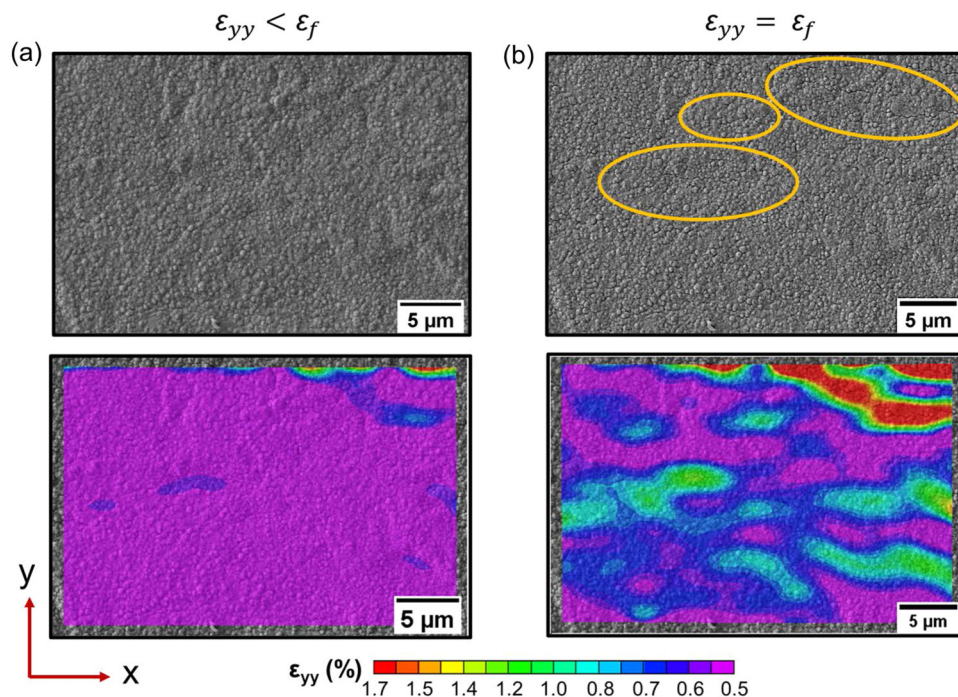


FIG. 4. SEM micrograph of the film surface ($h = 300$ nm) with the DIC map (a) before and (b) at the onset of cracking (regions marked show the cracks developed).

for the 900 nm films. Crack initiation was found to occur after a critical value of strain, which was itself a function of the film thickness. ϵ_f was found to be $\sim 0.8\%$, 0.8% , and 0.3% for the 300, 600, and 900 nm film thicknesses, respectively. This implies that the

initiation of cracks occurs at lower strains for thicker films. With continued straining, crack density increased and reached a plateau, which is expected, as also described by Cordill and co-workers.^{15,16} The strain at which cracks reached saturation spacing also had the

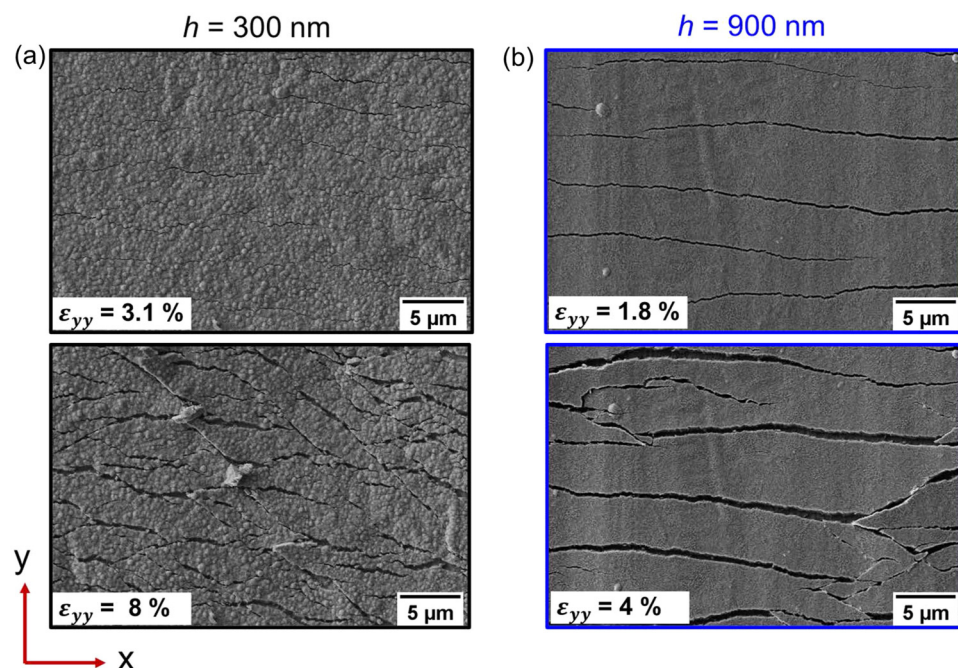


FIG. 5. Micrographs showing the distribution of cracks on the film surface after saturation strain and at the final stage of deformation where interface delamination and buckling occurred, for (a) 300 and (b) 900 nm film thicknesses.

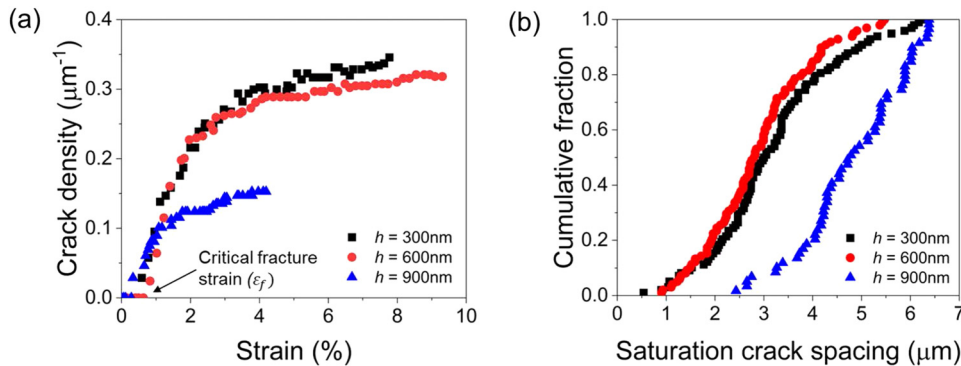


FIG. 6. (a) Crack density vs strains calculated from DIC for different film thicknesses. (b) Cumulative distribution of crack spacing measured at the saturation strain values for different film thicknesses.

same trend, with $\epsilon_{sat} \sim 3.4\%$, 3.8% , and 1.4% for the films of thickness 300, 600, and 900 nm, respectively. These strains were higher and represented the point at which the Ni substrate had undergone substantial plastic deformation. For a particular value of strain, the measured crack density was found to be lower for thicker films at crack saturation, and the saturation crack spacing higher. On the other hand, the crack opening width was larger for the thick films as compared to thinner films [Fig. 6(b)]. The measured values of crack density, initiation fracture strain, crack saturation strain, fracture strength, and crack spacing distribution for all the films are listed in Table I. The tensile fracture strength for the BaTiO₃ nanocrystalline films was found to be one order higher than the fracture strength of the BaTiO₃ polycrystalline bulk counterpart, which was reported to be in the range of 40–80 MPa.³⁷ One contributing factor could be the presence of compressive residual stresses in them. However, in comparison with the failure strength in compression of BaTiO₃ micropillars on single crystals where the failure strength value ranges from 1 to 5 GPa for different specimen sizes, the thin films failed at lower stresses.^{2,38} To the best of our knowledge, this is the first study to additionally report interface shear strengths for BaTiO₃ thin films on metallic substrates (Table I). Interface shear strengths, of the order of 0.23–0.43 GPa, were observed for 300 and 600 nm films, respectively, which is considerably lower than those reported for other metal ceramic interfaces (~ 1.5 GPa).^{13,30} The 900 nm films showed a much lower interface strength of about 0.12 GPa. Due to the similar range of fracture strengths and saturation crack spacings for the 300 and 600 nm films, the interface shear strength was nearly double in the 600 nm film, since it scales proportional to the film thickness as given in Eq. (5).

The critical flaw size (a_{min}) to initiate cracking (Table I) was determined [Eq. (8)] from the measured values of thin film fracture

toughness, and the fracture stresses. Note that K_{IC} is determined from the microcantilever beams and the fracture strength is from the shear lag experiments,

$$a_{min} = \frac{1}{\pi} \left(\frac{K_{IC}}{\sigma_f} \right)^2. \quad (8)$$

Critical flaw size calculated using Eq. (8) shows an increase with increase in film thickness, indicative of the accumulation of defects during the growth. The critical flaw size (in the form of microcracks and porosities) was estimated to be ~ 70 nm for the 300 and 600 nm thick films while it was estimated to be ~ 400 nm for the 900 nm thick films. Such large defects were indeed detected on the surface of the 900 nm thick films, leading to the early onset of failure and lower damage tolerance. While the residual stress is measured to be the same for all the film thicknesses studied, the fracture strength turns out to be different, indicative of the increasingly larger growth defects with increasing thickness. The fracture strength reported in Table I includes the residual stress in the film as well. The origin and type of growth defects are a function of multiple variables during the deposition process.³⁹ Detailed discussion on the defect formation is not included here since it is beyond the scope of this work. The maximum defect size is typically limited by the film thickness.⁴⁰ In our study, the maximum flaw size calculated is well within the film thickness for each case. The residual stresses being a constant for all the films, and compressive in nature, cannot be responsible for the difference in flaw size as a function of film thickness. Thus, the reduced damage tolerance of thicker films can be attributed to growth defects that occur during the deposition process and suggest that minimizing them can help improve the fracture resistance of these films.

TABLE I. Summary of the results measured from the shear lag tests (error bars represent standard error of mean from three samples).

Film thickness, h (nm)	Critical fracture strain, ϵ_f (%)	Fracture strength, σ_f (GPa)	Crack saturation strain, ϵ_{sat} (%)	Saturation crack spacing, λ (μm)	Interface shear stress, τ_{ISS} (GPa)	Critical flaw size, a_{min} (nm)
300	0.8 ± 0.04	0.95 ± 0.05	3.4 ± 0.1	3.0 ± 0.2	0.23 ± 0.04	70 ± 8
600	0.8 ± 0.01	0.93 ± 0.01	3.8 ± 1.0	2.8 ± 0.02	0.44 ± 0.01	70 ± 1
900	0.3 ± 0.02	0.40 ± 0.02	1.4 ± 0.4	6.9 ± 1.5	0.13 ± 0.03	389 ± 51

To summarize, it is shown that multi-scale *in situ* micromechanical characterization tools are needed to quantify the damage tolerance of ferroelectric thin films, an essential component of their application in service. Such shear lag tests can be further extended to mechanical and thermal fatigue cycles to determine the impact of film thickness on fatigue failure. Thin film engineers should consider the changes in mechanical performance as a function of film thickness while designing strategies for their deployment in devices at miniature length scales.

IV. CONCLUSION

Barium titanate thin films of different thickness ($h = 300, 600,$ and 900 nm) were deposited on Ni substrates using pulsed laser deposition, and their fracture behavior was studied in free-standing and attached forms. Microstructural characterization, grain size, and residual stress measurement revealed the nanocrystalline nature and the presence of significant compressive residual stresses in all the films, with magnitudes being similar independent of the film thickness. Fracture toughness value of $0.4 \text{ MPa}\sqrt{m}$ was measured for the free-standing thin films from the microcantilever bend tests, which was found to be 67% lower than single crystal fracture toughness. However, the fracture behavior of these BaTiO_3 thin films attached to the substrate tested using *in situ* shear lag tests did show a thickness dependence. Full field strain maps were used to detect the initiation of cracks perpendicular to the loading direction. Critical strain for the onset of cracking was found to decrease with increasing film thickness, with 0.8% and 0.3% for the film thickness of 300 and 900 nm, respectively. Thin films up to 600 nm thickness possessed 130% higher damage tolerance in terms of fracture strength compared to thick films of 900 nm thickness, the latter initiating cracks at the defect features present in them. Crack density increased on further straining and reached saturation, beyond which the film delaminated at the interface due to incompatibility of strains with the plastically deforming metallic substrate. The fracture strength and fracture toughness measurements were combined to estimate a flaw size of less than 70 nm in the 300 and 600 nm films and a flaw size of 400 nm in the 900 nm films, which thereby reduced the damage tolerance as the cracks initiated from these flaws. Therefore, it was shown that strong, adherent BaTiO_3 films can be grown up to 600 nm thickness with sufficient damage tolerance.

ACKNOWLEDGMENTS

The authors acknowledge the Max-Planck Society Partner Group Project (No. 17MAX001) for the financial support. The authors also acknowledge the use of central and departmental facilities—PLD, Nanoindenter, XRD, and Dual beam FIB-SEM—at IIT Bombay for the experimental support.

AUTHOR DECLARATIONS

Conflict of Interest

The authors have no conflicts to disclose.

Author Contributions

N. G. Mathews: Data curation (lead); Formal analysis (lead); Investigation (lead); Methodology (equal); Writing – original draft (equal). **A. K. Saxena:** Investigation (supporting); Methodology (supporting). **N. Venkataramani:** Investigation (equal); Supervision (equal); Writing – review and editing (equal). **G. Dehm:** Formal analysis (equal); Funding acquisition (equal); Writing – review and editing (equal). **B. N. Jaya:** Conceptualization (lead); Formal analysis (equal); Funding acquisition (lead); Project administration (lead); Supervision (lead); Writing – original draft (equal); Writing – review and editing (lead).

DATA AVAILABILITY

The data that support the findings of this study are available from the corresponding author upon reasonable request.

REFERENCES

- 1 J. Gao, D. Xue, W. Liu, C. Zhou, and X. Ren, *Actuators* **6**, 1–20. (2017).
- 2 N. G. Mathews, A. K. Saxena, C. Kirchlechner, G. Dehm, and B. N. Jaya, *Scr. Mater.* **182**, 68 (2020).
- 3 M. Cernea, *J. Optoelectron. Adv. Mater.* **6**, 1349 (2004).
- 4 L. Mazet, S. M. Yang, S. V. Kalinin, S. Schamm-Chardon, and C. Dubourdieu, *Sci. Technol. Adv. Mater.* **16**, 036005 (2015).
- 5 Y. Yang, Z. Wang, J. Li, and D. Viehland, *J. Nanomater.* **756319**, 1–5 (2010).
- 6 G. Niu, S. Yin, G. Saint-Girons, B. Gautier, P. Lecoœur, V. Pillard, G. Hollinger, and B. Vilquin, *Microelectron. Eng.* **88**, 1232 (2011).
- 7 L. Qiao and X. Bi, *Ferroelectric- Material Aspects* (Intechopen, 2011), pp. 363–388.
- 8 T. Lipinsky, J. Schubert, and C. Buchal, *J. Opt. Soc. Am. B* **22**, 913 (2005).
- 9 H. Elangovan, M. Barzilay, S. Seremi, N. Cohen, Y. Jiang, L. W. Martin, and Y. Ivry, *ACS Nano* **14**, 5053 (2020).
- 10 G. Dong, S. Li, M. Yao, Z. Zhou, Y.-Q. Zhang, X. Han, Z. Luo, J. Yao, B. Peng, Z. Hu, H. Huang, T. Jia, J. Li, W. Ren, Z.-G. Ye, X. Ding, J. Sun, C.-W. Nan, L.-Q. Chen, J. Li, and M. Liu, *Science* **366**, 475 (2019).
- 11 H. Jin, W. Y. Lu, M. J. Cordill, and K. Schmidegg, *Exp. Mech.* **51**, 219 (2011).
- 12 M. J. Cordill, A. Taylor, J. Schalko, and G. Dehm, *Metal. Mater. Trans. A* **41**, 870 (2010).
- 13 D. C. Agrawal and R. Raj, *Acta Metall.* **37**, 1265 (1989).
- 14 G. Dehm, B. N. Jaya, R. Raghavan, and C. Kirchlechner, *Acta Mater.* **142**, 248 (2018).
- 15 M. J. Cordill, F. D. Fischer, F. G. Rammerstorfer, and G. Dehm, *Acta Materialia* **58**, 5520 (2010).
- 16 A. A. Taylor, M. J. Cordill, and G. Dehm, *Philos. Mag.* **92**, 3363 (2012).
- 17 B. Völker, C. Du, H. Fager, H. Rueß, R. Soler, C. Kirchlechner, G. Dehm, and J. M. Schneider, *Surf. Coat. Technol.* **390**, 125645 (2020).
- 18 K. Yamamoto, Y. Kawaguchi, T. Yasunaga, and T. Sato, *Surf. Coat. Technol.* **113**, 227 (1999).
- 19 S. Djaziri, S. Gleich, H. Bolvardi, C. Kirchlechner, M. Hans, C. Scheu, J. M. Schneider, and G. Dehm, *Surf. Coat. Technol.* **289**, 213 (2016).
- 20 M. Alfreider, J. Zechner, and D. Kiener, *JOM* **72**, 4551 (2020).
- 21 A. K. Mishra, H. Gopalan, M. Hans, C. Kirchlechner, J. M. Schneider, G. Dehm, and B. N. Jaya, *Acta Mater.* **228**, 117777 (2022).
- 22 K. Matoy, H. Schönherr, T. Detzel, T. Schöberl, R. Pippin, C. Motz, and G. Dehm, *Thin Solid Films* **518**, 247 (2009).
- 23 B. N. Jaya, C. Kirchlechner, and G. Dehm, *J. Mater. Res.* **30**, 686 (2015).
- 24 N. G. Mathews, A. K. Mishra, and B. N. Jaya, *Theor. Appl. Fract. Mech.* **115**, 103069 (2021).
- 25 *ASTM C20-00* (ASTM International, West Conshohocken, PA, 2015), p. 1.
- 26 W. C. Oliver and G. M. Pharr, *J. Mater. Res.* **7**, 1564 (1992).

- ²⁷R. Raj, A. Saha, L. An, D. P. H. Hasselman, and P. Ernst, *Acta Mater.* **50**, 1165 (2002).
- ²⁸V. C. Jobin, R. Raj, and S. L. Phoenix, *Acta Metall. Mater.* **40**, 2269 (1992).
- ²⁹G. Singh, Y. Yu, F. Ernst, and R. Raj, *Acta Mater.* **55**, 3049 (2007).
- ³⁰P. Scherrer, in *Kolloidchemie Ein Lehrbuch*, edited by R. Zsigmondy (Springer, Berlin, 1912), pp. 387–409.
- ³¹F. Cordero, *J. Appl. Phys.* **123**, 094103 (2018).
- ³²G. A. Schneider and V. Heyer, *J. Eur. Ceram. Soc.* **19**, 1299 (1999).
- ³³S. Brinckmann, C. Kirchlechner, and G. Dehm, *Scr. Mater.* **127**, 76 (2017).
- ³⁴D. E. J. Armstrong, A. J. Wilkinson, and S. G. Roberts, *J. Mater. Res.* **24**, 3268 (2009).
- ³⁵B. Gong, D. Frazer, B. Shaffer, H. C. Lim, P. Hosemann, and P. Peralta, *J. Nucl. Mater.* **557**, 153210 (2021).
- ³⁶L. B. Freund and S. Suresh, *Thin Film Materials: Stress, Defect Formation and Surface Evolution* (Cambridge University Press, 2003).
- ³⁷J. M. Blamey and T. V. Parry, *J. Mater. Sci.* **28**, 4988 (1993).
- ³⁸L. Yingwei, C. Kangjie, L. Chang, J. Peng, Q. Ke, G. Peng, W. Jie, R. Fuzeng, S. Qingping, C. Longqing, and L. Jiangyu, *Proc. Natl. Acad. Sci. U.S.A.* **118**, e2025255118 (2021).
- ³⁹P. Panjan, A. Drnovšek, P. Gselman, M. Čekada, and M. Panjan, *Coatings* **10**, 447 (2020).
- ⁴⁰P. Wellner, O. Kraft, G. Dehm, J. Andersons, and E. Arzt, *Acta Mater.* **52**, 2325 (2004).